Inorganic Chemistry
Article
pubs.acs.org/IC

Syntheses and Electronic Structure of Bimetallic Complexes Containing a Flexible Redox-Active Bridging Ligand

Stacey Lindsay,[†] Siu K. Lo,[†] Oliver R. Maguire,[†] Eckhard Bill,[‡] Michael R. Probert,[†] Stephen Sproules,[§] and Corinna R. Hess*[,†]

[†]Department of Chemistry, University of Durham, South Rd, Durham, DH1 3LE, United Kingdom
[‡]Max-Planck-Institut für Chemische Energiekonversion, Stiftstrasse 34-36, D-45470 Mülheim an der Ruhr, Germany
[§]School of Chemistry and Photon Science Institute, The University of Manchester, Oxford Road, Manchester M13 9PL, United Kingdom

Ⓢ *Supporting Information*

ABSTRACT: The new ligand $\mathbf{L}^1$, 1-*N*,1-*N*-bis(pyridine-2-ylmethyl)-3-*N*-(pyridine-2-ylmethylidene)benzene-1,3-diamine, was synthesized as a platform for the study of bimetallic complexes containing redox-active ligands. The asymmetric $\mathbf{L}^1$ contains a redox-active α-iminopyridine unit bridged to redox-inert bis(2-pyridylmethyl)amino counterpart and offers two distinct coordination sites. The coordination chemistry of $\mathbf{L}^1$ with Fe, Cu, and Zn was examined. Reaction with zinc afforded the asymmetric binuclear complex $[(\mathrm{L}^1)\mathrm{Zn}_2\mathrm{Cl}_4]$ (**1**), whereas the symmetric $[(\mathrm{L}^1)_2\mathrm{Fe}_2(\mathrm{OTf})_2](\mathrm{OTf})_2$ (**2**) and $[(\mathrm{L}^1)_2\mathrm{Cu}_2](\mathrm{OTf})_4$ (**3**) were isolated in reactions with iron and copper. Both metal- and ligand-centered redox processes are available to the series of metal compounds. EPR and Mössbauer spectroscopy and magnetic susceptibility studies establish that both **2** and **3** are paramagnetic; the vanishingly small ferromagnetic interaction produces decoupled high-spin $\mathrm{Fe}^{\mathrm{II}}$ ($S = 2$) ions in **2**. DFT calculations provide further insight into the nature of the exchange interactions in the dimeric systems.

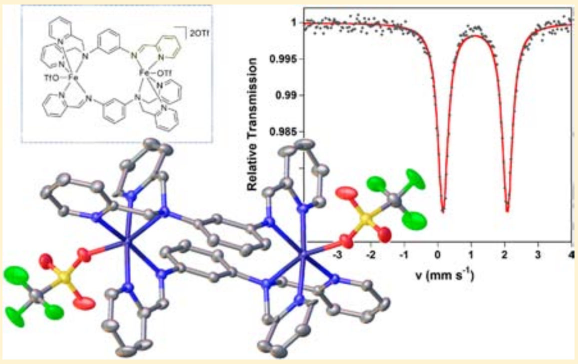

■ INTRODUCTION

The coordination chemistry of redox-active ligands has received considerable attention in recent years.[1] Metal complexes containing molecules such as the α-diimines, dioxolenes, and dithiolenes have been shown to not only defy conventional oxidation state assignments but exhibit unique electronic structures and rich chemistry.[2,3] Notably, the additional electron storage site afforded by the coordinated organic molecules can be advantageous for reactivity:[4] among the examples, ligand-centered redox processes have been implicated in C−C bond formation, alkene addition, and nitrene transfer reactions by transition metal and actinide complexes containing the aforementioned noninnocent moieties.[5−10]

Examples of bimetallic complexes containing redox-active ligands are fewer but offer further intrigue with respect to both reactivity and magnetism. The most common binuclear motif consists of two metal ions connected by a redox-active bridge that directly moderates exchange interactions between the sites.[11−13] These, predominantly symmetric, compounds have attracted attention due to their relevance for molecular electronics. Other examples include the dimeric $[\mathrm{Fe(TIM)}]_2$ (TIM = 2,3,9,10-tetramethyl-1,4,8,11-tetraazacyclotetradeca-1,3,8,10-tetraene) in which ligand radicals contribute to metal−metal bond formation and mixed valency.[14] Imido-bridged Zr and Ta dimers containing redox-active [NNN] and [ONO] pincer-type ligands also have been isolated;[10,15] the ligand plays a key role in oxidative formation of diazenes from the Ta_2 complex.[16] The latter example nicely illustrates that the electron storage capabilities of ligands can provide a powerful tool for multielectron transformations. However, the ramifications for the reactivity of binuclear compounds containing organic cofactors have yet to be fully explored.

We have now synthesized the asymmetric ligand $\mathbf{L}^1$ (1-*N*,1-*N*-bis(pyridine-2-ylmethyl)-3-*N*-(pyridine-2-ylmethylidene)-benzene-1,3-diamine; Scheme 1), as part of our initial efforts to explore the redox properties and reactivity of binuclear compounds containing redox-active ligands. In contrast to the aforementioned binuclear systems, $\mathbf{L}^1$ was designed with two distinct coordination sites, supplied by an α-iminopyridine and a bis(2-pyridylmethyl)amino group. The two-electron redox series available to α-iminopyridines, as a consequence of low-lying π^* orbitals, previously has been established,[17] whereas the pyridylmethylamino groups serve as innocent counterparts. The divergent nature of the two functional groups offers a strategy for selective reduction of one site in a binuclear complex, thus permitting mixed valency unconstrained by the accessibility of a particular metal oxidation state. In the case of

Received: September 26, 2012
Published: December 26, 2012

Scheme 1. Two-Electron Redox Series for the α-Iminopyridine Group with Characteristic Bond Distances (Angstroms)[17]

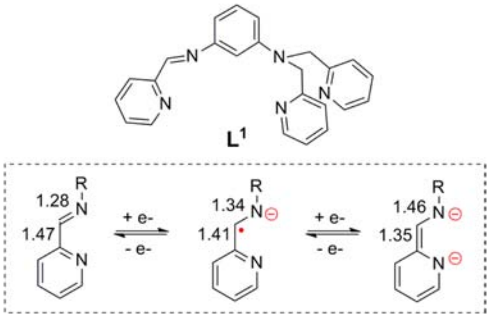

ligand-centered reduction, as opposed to metal-centered reduction, mixed valency refers to 'formal' rather than 'physical' oxidation states[18] but equally describes charge localization in the bimetallic complex.

The coordination chemistry of **L**^{1} with Fe, Cu, and Zn is described herein. The series of metal complexes includes both symmetric and asymmetric binuclear complexes. Electrochemical measurements provide an indication of the nature of the redox processes available to these complexes. The **L**$^1{}_2$−Cu_2 and **L**$^1{}_2$−Fe_2 complexes were further characterized by spectroscopic, magnetic susceptibility, and DFT computational studies, which denote weak ferromagnetic coupling mediated by **L**^{1}.

EXPERIMENTAL SECTION

Iron trifluoromethanesulfonate was purchased from Strem Chemicals; all other reagents were obtained from Sigma Aldrich and used as received. Metal compounds were synthesized in an inert atmosphere glovebox, under nitrogen, using anhydrous solvents. Solvents were dried by passage over activated alumina columns from Innovative Technology, Inc. (Amesbury, MA) and stored over activated 3 Å molecular sieves.

(3-Aminophenyl)carbamic Acid *tert*-Butyl Ester (I). Synthesis of the BOC-protected 1,3-benzenediamine was analogous to procedures previously described.[19] A solution of di-*tert*-butyl-dicarbonate (10.6 mL; 0.046 mol) in 1,4-dioxane (15 mL) was added dropwise to a solution of *m*-phenylenediamine (5.00g; 0.046 mol) in 1,4-dioxane (15 mL). Triethylamine (6.4 mL; 0.046 mol) was then added to the reaction mixture, and the solution was heated at 60 °C for 24 h. Solvent was removed in vacuo to yield a red-brown oil. Crude product was purified via flash column chromatography (2:3 ethyl acetate/hexanes; R_f = 0.2) to give the desired product, (3-aminophenyl)carbamic acid *tert*-butyl ester (6.5 g, 67% yield).

^{1}H NMR (400 MHz, $CDCl_3$): δ 7.04 (t, *J* = 9 Hz, 1H), 6.97 (s, 1H), 6.55 (ddd, *J* = 8, 2, 1 Hz, 1H), 6.37 (br, 1H), 6.37 (ddd, *J* = 8, 2, 1,1H), 3.67 (s, br, 2H), 1.51 (s, 9H). ^{13}C NMR (100 MHz, $CDCl_3$): δ 152.8, 147.4, 139.5, 129.8, 110.0, 108.8, 105.3, 80.5, 28.5.

{3-[Bis(pyridine-2-ylmethyl)amino]phenyl}amino-2,2-dimethylpropanoate (IIb). To a solution of (3-aminophenyl)carbamic acid *tert*-butyl ester (**I**: 4.00 g; 0.019 mol) in anhydrous ethanol (60 mL) was added Na_2CO_3 (8.14 g; 0.077 mol). 2-(Chloromethyl)-pyridine hydrochloride (6.3 g; 0.038 mol) was then added, and the mixture was heated to reflux at 80 °C for 24 h. The resulting brown suspension was filtered, and the solvent was removed in vacuo to yield a brown oil. The brown oil was diluted with CH_2Cl_2 (40 mL) and treated with 2 M NaOH (50 mL). Product was extracted with CH_2Cl_2 (3 × 50 mL), then the organic layer was washed with brine (2 × 50 mL) and dried over $MgSO_4$, and the CH_2Cl_2 was removed under vacuum. The crude product was run through a silica plug (125 cm^3 silica; ethyl acetate; R_f = 0.2) to give the desired product as an orange oil (4.1 g, 44% yield).

^{1}H NMR (400 MHz, $CDCl_3$): δ 8.58 (ddd, *J* = 5, 2, 1 Hz, 2H), 7.62 (td, *J* = 8, 2 Hz, 2H), 7.25 (d, 2H), 7.16 (ddd, *J* = 7, 5, 1 Hz, 2H), 7.07 (t, *J* = 8 Hz, 1H), 6.89 (br, 1H) 6.58 (t, *J* = 2 Hz, 1H), 6.38 (dd, *J* = 8, 3 Hz, 1H), 6.35 (s, br, 1H) 4.79 (s, 4H) 1.46 (s, 9H). ^{13}C NMR (176 MHz, $CDCl_3$): δ 158.9, 152.8, 149.8, 149.1, 139.6, 137.0, 130.0, 122.2, 121.1, 108.1, 107.8, 102.8, 80.42, 57.31, 28.46. MS (LRMS$^+$; ESI; *m*/*z*): 391.4 [M + H], 185.2 [M$^+$ −2Me-Py], 102.2 [M$^+$ − (BOC + 2Me-Py)].

1-*N*,1-*N*-Bis(pyridin-2-ylmethyl)benzene-1,3-diamine (III). **IIb** (1.00 g; 2.56 mmol) was dissolved in ethyl acetate (30 mL) and then treated dropwise with 12 M HCl (10 mL). The reaction mixture was left to stir for 1 h. The resultant solution was combined with 5 M NaOH (50 mL), and the organic layer was extracted with CH_2Cl_2 (3 × 50 mL). Solvent was removed in vacuo to yield the brown solid **III** (0.7 g, 98% yield).

^{1}H NMR (400 MHz, $CDCl_3$): δ 8.58 (ddd, *J* = 5, 2, 1 Hz, 2H) 7.62 (td, *J* = 8, 2 Hz, 2H) 7.28 (d, 2H) 7.16 (dd, *J* = 7, 5 Hz, 2H) 6.95 (t, *J* = 8 Hz, 1H) 6.14 (dd, *J* = 8, 2 Hz, 1H), 6.09 (dd, *J* = 8, 2 Hz, 1H), 6.02 (t, *J* = 2 Hz, 1H) 4.78 (s, 4H), 3.51 (s, 2H). ^{13}C NMR (176 MHz, $CDCl_3$): δ 159.2, 149.8, 149.6, 147.7, 137.0, 130.3, 122.1, 121.0, 104.9, 103.7, 99.49, 57.38. MS (LRMS$^+$; ESI; *m*/*z*): 291.3 [M + H], 200.2 [M$^+$ − Me-Py], 109.2 [M$^+$ − 2Me-Py].

1-*N*,1-*N*-Bis(pyridine-2-ylmethyl)-3-*N*-(pyridine-2-ylmethylidene)benzene-1,3-diamine (L^1). A solution of 2-pyridinecarboxaldehyde (180 μL; 1.89 mmol) and **III** (0.50 g; 1.72 mmol) in dry toluene (90 mL) was heated to reflux at 120 °C, over 4 Å molecular sieves, under an argon atmosphere for 5 h. Solvent was removed in vacuo to give the yellow solid **L**^{1} (0.60 g, 90% yield).

^{1}H NMR (400 MHz, $CDCl_3$): δ 8.68 (d, *J* = 4 Hz, 1H), 8.59 (d, *J* = 4 Hz, 2H), 8.51 (s, 1H) 8.11 (d, *J* = 8 Hz, 1H) 7.78 (t, *J* = 8 Hz, 1H) 7.63 (t, *J* = 7 Hz, 2H) 7.34 (td, *J* = 6 Hz, 1H) 7.29 (d, *J* = 8 Hz, 2H) 7.17 (m, 3H) 6.64 (m, 3H) 4.85 (s, 4H). ^{13}C NMR (176 MHz, $CDCl_3$): δ 160.3, 158.5, 154.5, 152.3, 149.7, 149.7, 149.3, 136.8, 136.6, 130.0, 125.0, 122.1, 122.0, 120.8, 110.9, 109.2, 105.9, 57.1. MS (LRMS$^+$; ESI; *m*/*z*): 380.6 [M + H]. An accurate mass of the molecule was determined using high-resolution MS and found to be within 6 ppm (HRMS; ASAP; *m*/*z*: 380.1898 [M + H]). UV−vis: λ_{max}, nm (ε, M^{-1} cm^{-1}) in CH_2Cl_2: 254 (3.8 × 10^4).

[(L^1)Zn_2Cl_4] (1). Colorless $ZnCl_2$ (26 mg; 0.19 mmol) was added to a solution of **L**^{1} (36 mg; 0.09 mmol) in THF or MeCN (10 mL). The mixture was stirred overnight, and the resultant yellow precipitate was filtered to give **1** (43 mg, 70% yield). Diffraction-quality single crystals were obtained by slow evaporation of a concentrated solution of **1** in MeCN.

^{1}H NMR (700 MHz, CD_2Cl_2): δ 9.24 (d, *J* = 5 Hz, 2H), 9.01 (s, 1H), 8.81 (d, *J* = 5 Hz,1H), 8.27 (td, *J* = 8, 2 Hz, 1H) 8.08 (d, *J* = 8 Hz, 1H) 7.93 (m, 3H) 7.87 (ddd, *J* = 8, 5, 1 Hz, 1H), 7.52 (t, *J* = 6 Hz, 2H) 7.51 (d, *J* = 8 Hz, 2H) 7.40 (m, 3H). Anal. Calcd for $C_{24}H_{21}Cl_4N_5Zn_2$: C, 44.21; H, 3.25; N, 10.74. Found: C, 43.99; H, 3.25; N, 10.80. UV−vis: λ_{max}, nm (ε, M^{-1} cm^{-1}) in CH_2Cl_2: 262 (∼1.6 × 10^4), 331 (∼1.6 × 10^4).

[(L^1)$_2$$Fe_2(OTf)_2$](OTf)$_2$ (2). A suspension of Fe(OTf)$_2$ (23 mg, 0.065 mmol) in THF (5 mL) was added to a solution of **L**^{1} (25 mg; 0.066 mmol) in THF (5 mL; THF was stored over Na; the yield of product obtained was highly dependent on the quality of the reagents and solvent) upon which the mixture immediately turned green. The reaction mixture was stirred for 72 h, during which time a series of color changes was observed, from green to blue to black, with the appearance of a pink solid. The pink solid **2** was collected by filtration (26 mg, 54% yield), leaving a charcoal gray filtrate. Additional products of this reaction were not identified. Single crystals were obtained by slow diffusion of diethyl ether into a solution of **2** in MeCN.

Anal. Calcd for $C_{52}H_{42}N_{10}O_{12}S_4F_{12}Fe_2$: C, 42.58; H, 2.89; N, 9.55. Found: C, 42.37; H, 2.96; N, 9.61. UV−vis: λ_{max}, nm (ε, M^{-1} cm^{-1}) in MeCN: 515 (750).

[(L^1)$_2$$Cu_2$](OTf)$_4$ (3). In THF (5 mL) was dissolved **L**^{1} (25 mg; 0.066 mmol) and Cu(OTf)$_2$ (25 mg; 0.066 mmol). The solution was stirred overnight, resulting in a forest green suspension, which was filtered to give the green solid **3** (36 mg, 74% yield). Single crystals

Scheme 2. Synthesis of L^1

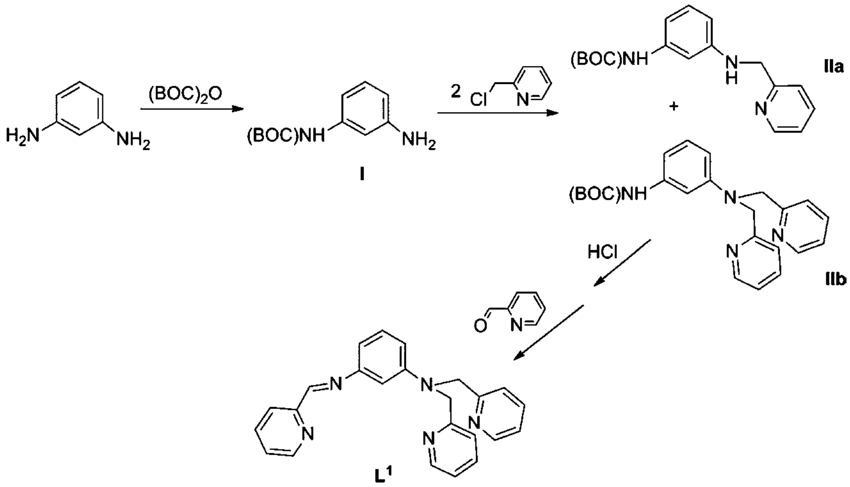

were obtained by slow diffusion of diethyl ether into an acetonitrile solution of **3**.

Anal. Calcd for $C_{52}H_{42}N_{10}O_{12}S_4F_{12}Cu_2$: C, 42.13; H, 2.86; N, 9.45. Found: C, 42.20; H, 3.01; N, 9.46. UV–vis: λ_{max}, nm (ε, M^{-1} cm^{-1}) in MeCN: 596 (520). MS (LRMS$^+$; ESI; m/z): 1333.3 [M − OTf], 592.2 [M − 2OTf], 221.2 [M − 4OTf].

Physical Measurements. NMR spectra were recorded on a Bruker Avance-400 (400 MHz ^{1}H, 100 MHz ^{13}C, 376 MHz ^{19}F) or a Varian VNMRS-700 (700 MHz ^{1}H, 176 MHz ^{13}C) spectrometer. Electronic spectra were recorded on a Perkin-Elmer Lambda 900 spectrophotometer. Diffuse reflectance spectra were obtained by illumination of the sample using an Energetiq LDLS EQ-99 broadband lamp and collected at 20° to the excitation using an Ocean Optics Maya Pro 2000 spectrometer. Data was recorded using the Ocean Optics software, and integration times were adjusted to afford maximum response of the spectrometer without saturation of the detector. Teflon was used as the white standard. Mass spectra were measured using a Waters TQD instrument for ESI (1 μL of a ~1 mg/mL sample in methanol or acetonitrile injected into a flow (0.2 mL/min) of methanol or acetonitrile; capillary voltage 3000 V, cone voltage 30 V) or on a *Xevo QToF* for high-resolution spectra (atmospheric pressure solids analysis probe ionization experiments (ASAP)). Microanalyses were carried out in the Chemistry Department at Durham University. Electrochemical measurements were carried out using an Autolab PG-STAT 30 potentiostat using a three-electrode cell equipped with a Pt working electrode and Pt wire counter and reference electrodes. Potentials are reported with reference to an internal standard of ferrocenium/ferrocene ($Fc^{+/0}$). Magnetic susceptibility data (2–290 K) were recorded using a SQUID magnetometer (MPMS7, Quantum Design) in a 1 T external field. Data were corrected for underlying diamagnetism using tabulated Pascal's constants and fit using julX (Dr. E. Bill). Mössbauer data were recorded on an alternating constant-acceleration spectrometer. The minimum experimental line width was 0.24 mm s^{-1} (full width at half-height). Sample temperature was maintained constant in an Oxford Instruments Variox or an Oxford Instruments Mössbauer-Spectromag 2000 cryostat, which is a split pair superconducting magnet system for applied fields (up to 8 T). The field at the sample is oriented perpendicular to the γ-beam. The ^{57}Co/Rh source (1.8 GBq) was positioned at room temperature inside the gap of the magnet system at a zero-field position. Isomer shifts are quoted relative to iron metal at 300 K; data were simulated using mfit (Dr. E. Bill). Multifrequency EPR measurements were carried out at the EPSRC National UK EPR Facility and Service in the Photon Science Institute at The University of Manchester. X-Band spectra were collected using a Bruker EMX Micro spectrometer, K-band spectra with a Bruker E580 spectrometer, and Q-band spectra on a Bruker EMX spectrometer. Simulations were performed using Bruker's Xsophe software package.[20]

Crystallography. Structure determinations were carried out from single-crystal X-ray diffraction data collected at 100 K using Cu Kα radiation (λ = 1.54178 Å) on a Bruker Pt135-CCD Proteum diffractometer with multilayer focusing optics or at 120 K using Mo Kα radiation (λ = 0.71073 Å) on a Bruker SMART 6K-CCD diffractometer. Sample temperature was controlled and maintained using an Oxford Cryosystems open-flow N_2 cooling device.[21] A series of narrow φ and/or ω scans (0.5° or 0.3°) was performed at various setting angles to maximize data coverage. Unit cell parameters were determined and refined inside the APEX2[22] software suite, and raw data were integrated using the SAINT program.[23] Structures were solved, refined, and publication material produced using the OLEX2[24] interface to the SHELXTL suite of programs.[25] All structures presented were affected, to variable degrees, by low-resolution data being achievable, due to crystal size and quality. This was also coupled in many cases with solvent and/or ligand disorder (further details are included in the crystallographic information files). In particular, the small size of **1** and the low crystal symmetry (P-1), coupled to the orientation of the sample, limited the completeness of the diffraction data for **1** at high resolution. In spite of the less than ideal completeness, diffraction data were collected to a θ_{max} of 68.33° with Cu Kα radiation, giving a data to parameter ratio of 4179/316. Lower than optimal completeness to high angle does marginally affect the accuracy of the derived parameters but is correctly reflected in the standard uncertainties recorded in the crystallographic information file and reported parameters herein.

Density Functional Theory (DFT) Calculations. All DFT calculations were performed with the ORCA program package.[26] Geometry optimizations of the complexes were performed at the B3LYP[27−29] level of DFT. The all-electron Gaussian basis sets were those developed by the Ahlrichs group.[30,31] Triple-ζ quality basis sets TZV(P) with one set of polarization functions on the metals and on the atoms directly coordinated to the metal center were used.[31] For the carbon and hydrogen atoms, slightly smaller polarized split-valence SV(P) basis sets were used that were of double-ζ quality in the valence region and contained a polarizing set of d functions on the non-hydrogen atoms.[30] Auxiliary basis sets used to expand the electron density in the resolution-of-the-identity (RI) approach were chosen,[32,33] where applicable, to match the orbital basis. SCF calculations were tightly converged (1×10^{-8} E_h in energy, 1×10^{-7} E_h in the density change, and 1×10^{-7} in maximum element of the DIIS error vector). Geometry optimizations for all complexes were carried out in redundant internal coordinates without imposing symmetry constraints. In all cases the geometries were considered converged after the energy change was less than 5×10^{-6} E_h, the gradient norm and maximum gradient element were smaller than 1×10^{-4} and 3×10^{-4} E_h $Bohr^{-1}$, respectively, and the root-mean square and maximum displacements of all atoms were smaller than 2×10^{-3}

Scheme 3. Synthesis of Compounds 1−3

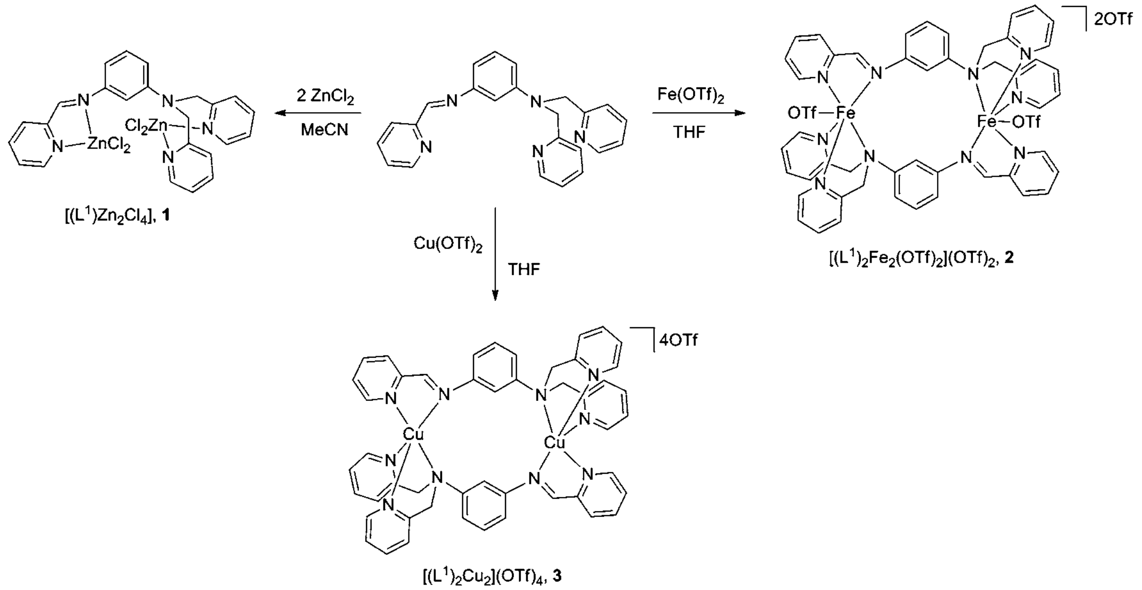

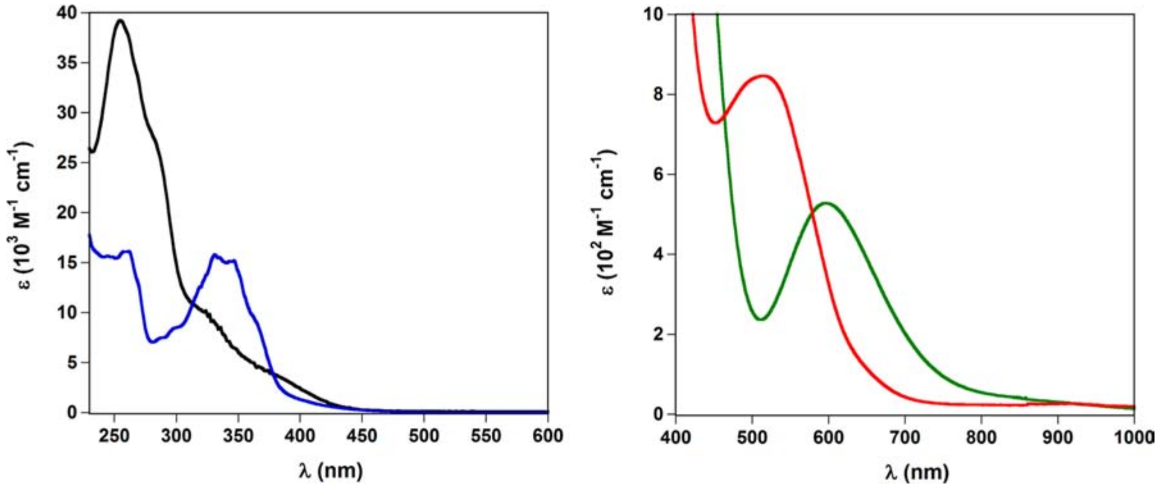

Figure 1. Comparison of the electronic spectra of L^1 (black) and **1** (blue) in CH_2Cl_2 (left) and spectra of **2** (red) and **3** (green) in MeCN (right).

and 4×10^{-3} Bohr, respectively. Orbital and spin density plots were created using GaussView.[34]

■ RESULTS AND DISCUSSION

Synthesis and Characterization. The new ligand $\mathbf{L^1}$ was designed as a bimetallic scaffold, endowed with a redox-active α-iminopyridine that could compete with coordinated metal ions for electrons (Scheme 1). The meta disposition of the bridging benzene moiety disfavors formation of a mononuclear complex, while the asymmetry of the molecule imposed by the disparate set of N-donor groups offers distinctive properties to each intended coordination site. Importantly, ligand-centered redox processes available to one coordination site could permit charge localization in reduced binuclear compounds. The two-electron redox series available to α-iminopyridines implies that both one- and two-electron charge-separated states could theoretically be accessed (Scheme 1). Thus, $\mathbf{L^1}$ offers an alternative strategy to the rare metal-based two-electron mixed-valence complexes.

$\mathbf{L^1}$ was synthesized in four steps starting from the commercially available *m*-phenylenediamine (Scheme 2). Reaction of the BOC-protected diamine (**I**)[19] with 2-(chloromethyl)pyridine hydrochloride affords a mixture of both the mono- (**IIa**) and the bis(pyridine-2-ylmethyl)benzene-1,3-diamine (**IIb**), which are readily separated by chromatography. Deprotection of **IIb** followed by reaction with 2-pyridinecarboxaldehyde cleanly generates the target molecule.

Subsequent examination of the coordination chemistry of $\mathbf{L^1}$ with Fe, Cu, and Zn allowed for comparison of the structural preferences and redox properties of the resultant first-row, late transition metal complexes. The unique electronic structures of iron−diimine complexes have been noted previously, with ligand-centered reduction predominantly favored over metal-centered reduction.[17,35,36] The paucity of low-valent iron compounds contrasts with the prevalence of monovalent copper, while the α-diimine group must be invoked in the reduction of Zn-containing compounds.

Bimetallic products were obtained in all reactions of $\mathbf{L^1}$ (Scheme 3), irrespective of the M:L ratio (2:1 or 1:1). However, an asymmetric binuclear complex, $[(L^1)Zn_2Cl_4]$ (**1**), was obtained in the reaction with $ZnCl_2$, while a symmetric dimer, $[(L^1)_2Fe_2(OTf)_2](OTf)_2$ (**2**), was the only identified

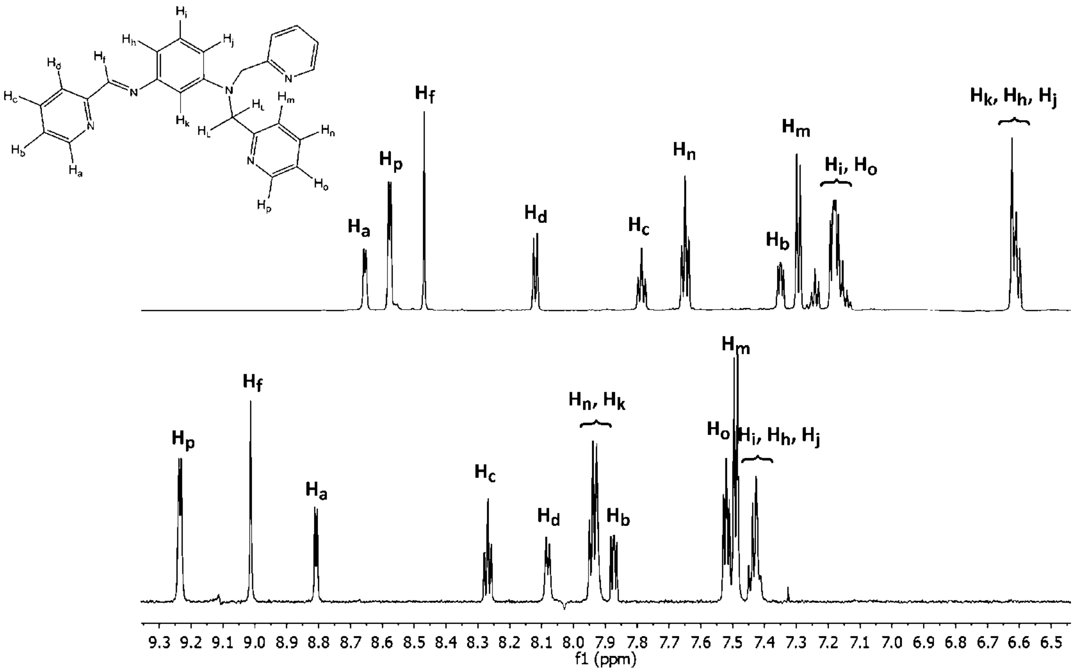

Figure 2. Overlay of the aromatic region of the ^{1}H NMR spectrum (700 MHz, CD_2Cl_2) of **L**^{1} (top) and **1** (bottom) with labeling scheme. Assignments based on COSY spectra (see Supporting Information).

product upon reaction of **L**^{1} with $Fe(OTf)_2$. An analogous dimeric copper-containing complex, $[(L^1)_2Cu_2](OTf)_4$ (**3**), also was obtained upon reaction of **L**^{1} with $Cu(OTf)_2$.

The binuclear zinc complex, $[(L^1)Zn_2Cl_4]$ (**1**), was obtained upon reaction of **L**^{1} with 2 equiv of $ZnCl_2$. Compound **1** is mildly soluble in CH_2Cl_2, and its electronic spectrum is clearly dissimilar to that of **L**^{1}, with a distinct absorption band at 331 nm (Figure 1). The proton resonances in the aryl region of the ^{1}H NMR spectrum of **1** in CD_2Cl_2 are shifted downfield significantly in comparison to the **L**^{1} spectrum (Figure 2).

Products obtained from the analogous reactions of **L**^{1} with $FeCl_2$ and $CuCl_2$ likewise proved highly insoluble, which obscured their characterization. Therefore, we sought alternative starting reagents to further investigate the ligand coordination chemistry. Addition of 1 equiv of $Fe(OTf)_2$ to a solution of **L**^{1} in THF led to precipitation of **2** as a pink solid. The series of color changes throughout the reaction suggests formation of various intermediates en route to or products in addition to **2**; the yield of **2** also did not exceed 54%. However, we have not identified any other products, and compound **2** was isolated in all reactions irrespective of the Fe:ligand stoichiometry (2:1, 1:1, 1:2 examined) when the reaction was carried out with $Fe(OTf)_2$.

The electronic spectrum of **2** features a single absorption band in the visible region, with λ_{max} = 515 nm (Figure 1), which we attribute to a metal-to-ligand charge transfer (MLCT) transition. The MLCT band in the solid state spectrum of **2** is slightly red shifted (λ_{max} = 523 nm) in comparison to the absorption band in acetonitrile solutions (Figure S7, Supporting Information). ^{19}F NMR of **2** shows a single, broad peak at −76 ppm (Figure S8, Supporting Information), indicative of noncoordinated triflate anions; signal broadening is a result of fast exchange of the triflate ions.[37−39] Therefore, although **2** was crystallized from $MeCN/Et_2O$ mixtures, we cannot exclude the possibility that in MeCN solutions the triflate ligands may be substituted by solvent molecules.

The analogous copper dimer, $[(L^1)_2Cu_2](OTf)_4$ (**3**), was synthesized in reactions with equimolar amounts of $Cu(OTf)_2$ and **L**^{1} in THF. The electronic spectrum of **3** in MeCN (Figure 1) exhibits an absorption band at λ_{max} = 596 nm (ε = 520 M^{-1} cm^{-1} ⇒ 260 M^{-1} cm^{-1} per Cu), which we assign to the Cu^{II} d−d transition. The absorbance value is within the typical range observed for related tetragonal Cu(II)−pyridine compounds.[40,41] Furthermore, a MLCT transition would be expected to occur at higher energy than for the corresponding diiron complexes.

Electrochemistry. Cyclic voltammograms (CV) of **L**^{1} and **1**−**3** are shown in Figure 3, and redox potentials are referenced versus the $Fc^{+/0}$ couple. The $[\mathbf{L}^1]/[\mathbf{L}^{1\bullet}]^-$ couple associated with the one-electron reduction of the α-diimine unit of **L**^{1} (Scheme 1) is observed at −0.86 V. The peak-to-peak separation is ~180 mV, suggesting structural rearrangement upon reduction.[42] A partially chemically reversible reduction is observed at $E_{1/2}$ = −1.31 V in the CV of **1** and readily described as ligand centered.

An irreversible oxidation is seen in the CV of **2** (Figure S9, Supporting Information) along with two closely spaced reduction events at −1.2 and −1.3 V, respectively. Reduction of the diiron complex occurs at slightly more negative potentials than observed for **L**^{1}. In contrast to **1**, both metal- and ligand-centered redox processes are feasible for **2**. Previous studies of iron complexes containing diimine ligands have demonstrated that reduction of the ligand commonly is favored over formation of low-valent metal oxidation states.[17,35,43] However, numerous intriguing possibilities exist with respect to the nature of the $[(L^1)_2Fe_2]^{4+/3+}$ and $[(L^1)_2Fe_2]^{3+/2+}$ couples and the distribution of two additional electrons among the four redox-active centers in **2**.

The $[(L^1)_2Cu_2]^{4+/3+}$ couple of **3** appears at a significantly more positive potential ($E_{1/2}$ = −0.44 V) than for **2**, denoting metal-centered reduction. This is in agreement with the observed trend of increasing metal character in a series of first-row bis(iminopyridine) complexes across the period from

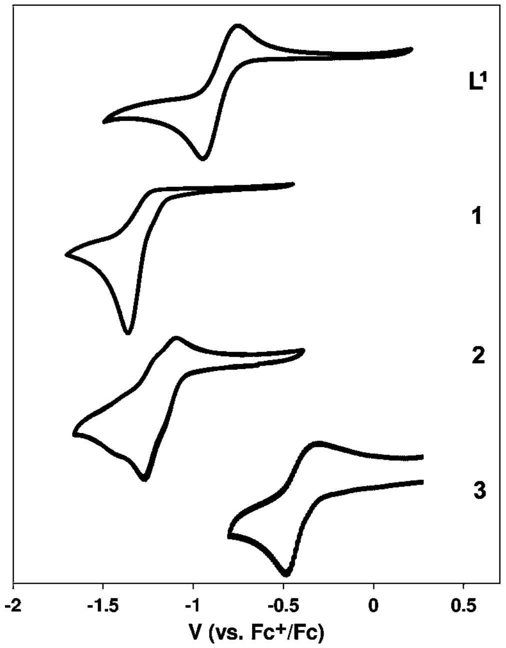

Figure 3. Cyclic voltammograms of $\mathbf{L}^1$ and **1**−**3**, 0.2 V s^{-1}, 0.1 M $[N(n\text{-}Bu)_4]PF_6$ ($\mathbf{L}^1$ and **1**) or $N(n\text{-}Bu)_4]OTf$ (**2** and **3**). CV of **1** was obtained in CH_2Cl_2, all others were obtained in MeCN.

Cr to Ni.[17] The lack of reversibility of this process can be rationalized by the expected changes in coordination geometry that typically accompany Cu^I formation. Further reduction of the dicopper complex is obscured by copper stripping beyond −0.75 V (Figure S9, Supporting Information).

Solid State Structures. The molecular structures of **1** and the complex cations $[(L^1)_2Cu_2]^{4+}$ and $[(L^1)_2Fe_2(OTf)_2]^{2+}$ are shown in Figures 4−6. The structure of **1**, although derived from less than optimal data completeness (see Experimental Section and CIF), substantiates the ability of $\mathbf{L}^1$ to accommodate two distinct metal coordination sites. The two zinc sites are distorted tetrahedral, with a constrained 80° bite angle imposed by the α-iminopyridine at Zn(1). The coordination geometry at the Zn(2) site is analogous to a related symmetric binuclear zinc complex, $[Zn_2(1,3\text{-tpbd})Cl_4]$ (1,3-tpbd = *N,N,N′,N′*-tetrakis(pyridine-2-ylmethyl)benzene-1,3-diamine),[44] with only a weak interaction between Zn(2) and the amino nitrogen (Zn(2)−N(3) = 2.624(2)). The chloride ligands prohibit close approach of the two zinc ions, leading to a Zn···Zn separation of ∼5.7 Å.

In the iron and copper dimers each metal ion is coordinated by an α-iminopyridine group of one $\mathbf{L}^1$ unit and the bis(pyridylmethyl)amino group of a second ligand. Two solvatomorphs of $[(L^1)_2Fe_2(OTf)_2](OTf)_2$ were isolated (Figure 5 and Table 1, denoted by **2·4MeCN** and **2·2MeCN**), which differ in the orientation of the coordinated triflate ligand and the number of solvent molecules. The Fe^{II} centers in both structures are octahedral: the N atoms of the bis(pyridylmethyl)amino groups adopt a facial arrangement, the opposing face comprised of the α-iminopyridine, and a coordinated triflate anion (Fe−O ≈ 2.1 Å). The Fe−N bond distances are indicative of high-spin Fe^{II} centers, as would be expected given the coordinated triflate ion. The coordination geometry at the iron center coincides with the 'slipped' arrangement of the $\mathbf{L}^1$ bridging benzenes and a 7.5−7.7 Å separation between the two metal sites.

Each Cu^{II} site in **3** adopts a distorted square pyramidal geometry (τ = 0.06−0.12),[45] with lengthening of the $Cu-N_{im}$ bond (∼2.26 Å) along the Jahn−Teller axis. The bis(pyridylmethyl)amino group assumes a pincer-like arrangement, with two short $Cu-N_{py}$ (∼1.97 Å) bonds and one slightly longer $Cu-N_{am}$ (∼2.1 Å) bond. The pyridyl nitrogen of the α-iminopyridine supplies the fourth ligand of the square planar base ($Cu-N_4$ plane = 0.214 Å), which constrains the weakly coordinated axial imine nitrogen at a 77° $N_{py}-Cu-N_{im}$ angle. The two $\mathbf{L}^1$ benzene rings of the dicopper complex are

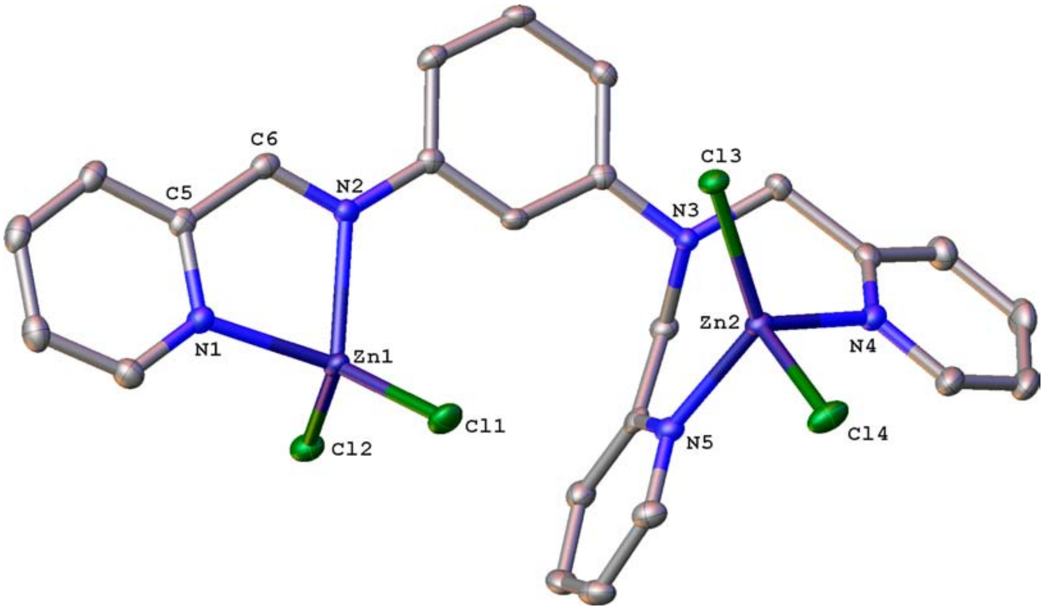

Figure 4. Structure of **1** (50% probability ellipsoids). Hydrogens omitted for clarity. Selected bond lengths (Angstroms) and angles (degrees): Zn1−Cl1 2.1917(5), Zn2−Cl3 2.2499(5), Zn1−Cl2 2.2176(6), Zn2−Cl4 2.2866(5), Zn1−N1 2.0714(16), Zn2−N3 2.624(2), Zn1−N2 2.088(2), Zn2−N4 2.067(2), Zn2−N5 2.070(2), N1−C5 1.352(3), C5−C6 1.468(3), N2−C6 1.287(3), N1−Zn1−N2 80.77(6), N4−Zn2−N5 99.23(7), Cl1−Zn1−Cl2 121.46(2), Cl3−Zn2−Cl4 103.56(2), Zn1···Zn2 5.6978(3).

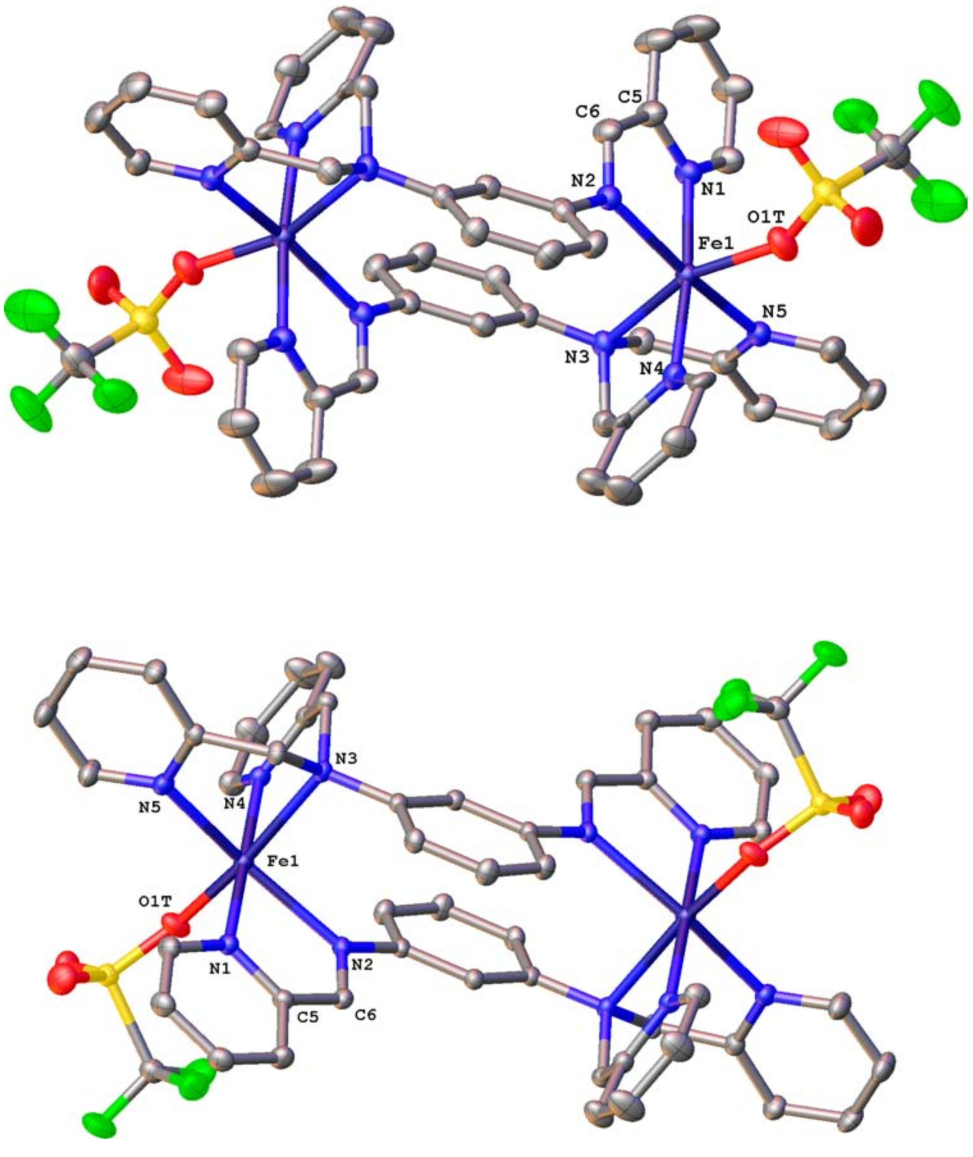

Figure 5. Molecular structure of **2·4MeCN** (top) and **2·2MeCN** (bottom); 50% probability ellipsoids. Hydrogen atoms and triflate counteranions have been omitted for clarity. Selected bond lengths (Angstroms) and angles (degrees). **2·4MeCN**: Fe−N1 2.177(3), Fe−N2 2.214(3), Fe−N3 2.321(2), Fe−N4 2.141(3), Fe−N5 2.161(3), Fe−O1T 2.103(2), N1−C5 1.351(4), N2−C6 1.273(4), C5−C6 1.460(5), N1−Fe−N2 75.96(9), N3−Fe−N4 78.64(9), N3−Fe−N5 76.22(9), N4−Fe−N5 91.2(1), N1−Fe−N4 174.36(9), N2−Fe−N5 166.8(1), N3−Fe−O1 162.2(1), Fe···Fe 7.4782(5). **2·2MeCN**: Fe−N1 2.170(1), Fe−N2 2.257(1), Fe−N3 2.350(1), Fe−N4 2.163(1), Fe−N5 2.180(1), Fe−O1T 2.113(1), N1−C5 1.353(2), N2−C6 1.286(2), C5−C6 1.463(2), N1−Fe−N2 75.73(4), N3−Fe−N4 77.92(4), N3−Fe−N5 75.40(5), N4−Fe−N5 88.76(5), N1−Fe−N4 177.46(5), N2−Fe−N5 159.46(5), N3−Fe−O1 165.37(4), Fe···Fe 7.7444(8).

nearly superimposed and within π-stacking distance (3.4−3.7 Å). The Cu···Cu separation consequently is significantly shorter (~6.9 Å) than in the diiron complex.

One consequence of the structural preferences of the different metal ion is the orientation of the α-iminopyridine group with respect to the benzene ring. The α-iminopyridine is coplanar with the benzene in **1** but rotated by 24° in **2·2MeCN**, 52° in **2·4MeCN**, and nearly orthogonal (~85°) in **3**. In all three structures, the C−N and C−C bond distances of the α-iminopyridine groups are as expected for the fully oxidized form (Scheme 1). The distances provide a benchmark for establishing ligand-centered reduction in future studies with these compounds.

Electronic Structure. The electronic structures of **2** and **3** and the nature of the metal−metal interactions in these complexes were probed by EPR and Mössbauer spectroscopies and SQUID magnetometry. These studies provide insight into the ability of $\mathbf{L^1}$ to modulate communication between the two coordination sites. The zero-field Mössbauer spectrum of **2** exhibits a single quadrupole doublet and establishes the electronic equivalence of the two metal centers (Figure 7). The fit of the data affords an isomer shift of δ = 1.12 mm s^{-1} and a quadrupole splitting of $|\Delta E_Q|$ = 1.93 mm s^{-1}, typical of high-spin Fe^{II} (S = 2) compounds.[46] Magnetic susceptibility measurements (Figure 8) show a temperature-independent magnetic moment in the range from 100 to 290 K, decreasing below 100 K to a value of ~4.8 μ_B. The effective magnetic moment of 7.9 μ_B at room temperature is higher than the spin-only value for two uncoupled S = 2 Fe centers (μ_{eff} = 6.9 μ_B for g = 2) but below the spin-only values of 8.9 μ_B for an S = 4 ground state arising from two strongly ferromagnetically

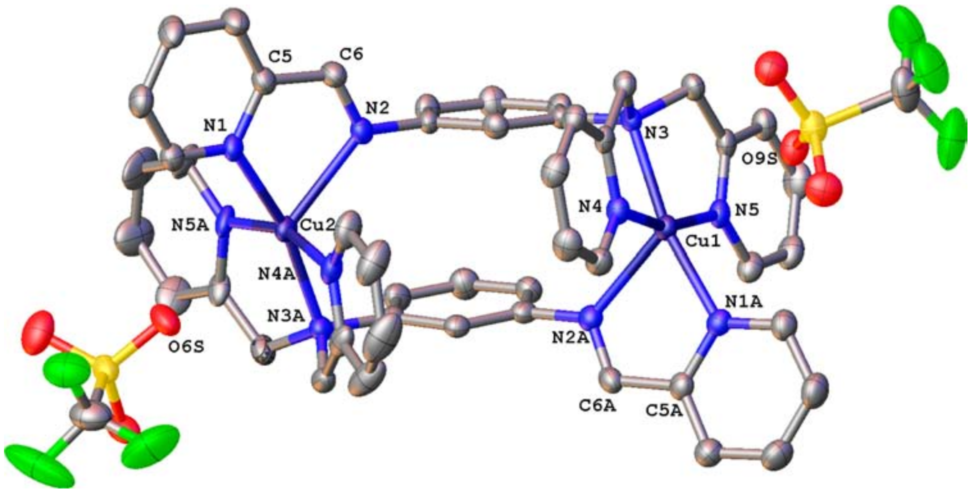

Figure 6. Structure of **3** (50% probability ellipsoids). Hydrogen atoms have been omitted, and only two triflate anions are shown for clarity. Selected bond lengths (Angstroms) and angles (degrees): Cu1−N1A 2.076(3), Cu1−N2A 2.247(3), Cu1−N3 2.106(3), Cu1−N4 1.978(3), Cu1−N5 1.968(3), Cu2−N1 2.042(3), Cu2−N2 2.282(3), Cu2−N3A 2.086(3), Cu2−N4A 1.975(3), Cu2−N5A$_{avg}$ 1.945(9), N1−C5 1.348(5), C5−C6 1.473(6), N2−C6 1.265(5), N1A−Cu1−N2A 76.7(1), N3−Cu1−N4 83.1(1), N3−Cu1−N5 82.9(1), N1A−Cu1−N3 166.7(1), N4−Cu1−N5 163.1(1), N1−Cu2−N2 76.9(1), N3A−Cu2−N4A 83.4(1), N3A−Cu2−N5A 85.5(4), N1−Cu2−N3A 166.3(1), N4A−Cu2−N5A$_{avg}$ 161.9(6), Cu1···Cu2 6.9283(8).

Table 1. Crystallographic Data for 1−3

	1	**2·4MeCN**[a]	**2·2MeCN**	**3**
chem. formula	$C_{24}H_{21}Cl_4N_5Zn_2$	$C_{62}H_{57}F_{12}Fe_2N_{15}O_{12}S_4$	$C_{56}H_{48}F_{12}Fe_2N_{12}O_{12}S_4$	$C_{52}H_{42}Cu_2F_{12}N_{10}O_{12}S_4$
fw	652.00	1672.17	1549.00	1482.28
cryst syst	triclinic	triclinic	triclinic	monoclinic
space group	*P*−1	*P*−1	*P*−1	*C*2/*c*
a (Å)	7.1827(2)	10.6568(2)	8.9929(11)	42.0617(8)
b (Å)	9.4410(2)	12.9150(2)	12.9736(18)	10.7977(2)
c (Å)	20.2740(4)	15.0100(3)	14.7541(16)	28.7341(5)
α (deg)	77.8560(10)	106.9800(10)	69.606(4)	90.00
β (deg)	87.9490(10)	109.4480(10)	86.687(5)	97.1390(10)
γ (deg)	72.3700(10)	97.5000(10)	76.892(4)	90.00
V (Å^3)	1280.35(5)	1802.68(6)	1571.0(3)	12949.0(4)
Z	2	1	1	8
cryst size (mm^3)	0.13 × 0.07 × 0.05	0.12 × 0.11 × 0.07	0.4 × 0.23 × 0.18	0.16 × 0.12 × 0.06
ρ_{calcd} (mg/mm^3)	1.691	1.540	1.637	1.521
μ (mm^{-1})	6.338	5.198	0.702	2.896
R_{int}	0.0357	0.0393	0.0228	0.0523
data/restraints/params	4179/0/316	5831/23/523	9589/22/483	10141/22/849
R_1 [$I \geq 2\sigma(I)$]	0.0241	0.0526	0.0388	0.0591
wR_2 [$I \geq 2\sigma(I)$]	0.0638	0.1550	0.1012	0.1730
R_1 [all data]	0.0247	0.0555	0.0451	0.0686
wR_2 [all data]	0.0645	0.1591	0.1061	0.1798
goodness-of-fit on F^2	1.058	1.092	1.069	1.088
$\Delta\rho_{min,max}$ (e Å^{-3})	−0.31, 0.34	−0.742, 0.591	−0.634, 1.023	−0.919, 1.424

[a] MeCN > 4, but could not be determined precisely due to high mobility of the final solvent molecule. [b] Observation criterion: $I > 2\sigma(I)$. $R_1 = \Sigma||F_o| - |F_c||/\Sigma|F_o|$. [c] $wR_2 = [\Sigma[w(F_o^2 - F_c^2)^2]/\Sigma[w(F_o^2)^2]]^{1/2}$, where $w = 1/\sigma^2(F_o^2) + (aP)^2 + bP$, $P = (F_o^2 + 2F_c^2)/3$. [d] GoF $= [\Sigma[w(F_o^2 - F_c^2)^2]/(n - p)]^{1/2}$.

coupled high-spin Fe^{II} ions. Data were fit according to the following spin Hamiltonian

$$H = -2J\hat{S}_1\cdot\hat{S}_2 + g\beta(\hat{S}_1 + \hat{S}_2)\cdot\vec{B} + \sum_{i=1,2} D\left[\hat{S}_{z,i}^2 - \frac{1}{3}S_i(S_i + 1) + \frac{E}{D}(\hat{S}_{x,i}^2 - \hat{S}_{y,i}^2)\right]$$

including exchange coupling and zero-field splitting terms, with $S_1 = S_2 = 2$. Fits with either J or D fixed at zero were included to assess the relative contribution of each parameter and yielded values for J = 0−0.2 cm^{-1} and $|D|$ = 14−22 cm^{-1}.[47] The best fit was obtained with g = 2.2, J = 0.04 cm^{-1}, $|D|$ = 19.7 cm^{-1}, and E/D = 0.26, denoting negligible interaction between the two iron centers in **2**. The magnitude of these parameters is confirmed by the absence of any EPR signal at Q-band frequency (∼34 GHz). The large single ion contribution to the zero-field splitting and its pronounced rhombicity shifts the

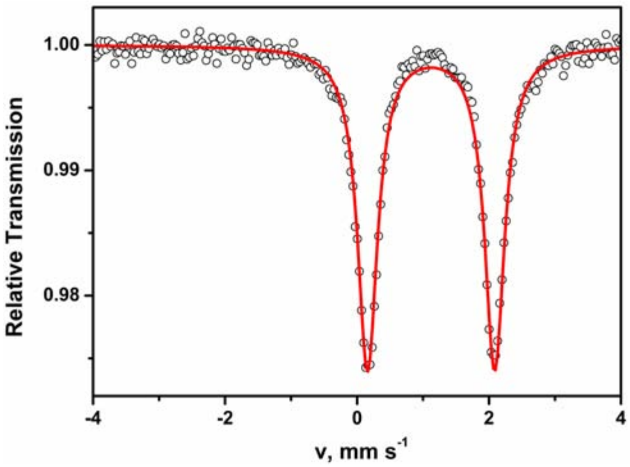

Figure 7. Zero-field Mössbauer spectrum of **2** at 80 K, where the open circles depict experimental data and the red line the fit (δ = 1.12 mm s^{-1}, |ΔE_Q| = 1.93 mm s^{-1}).

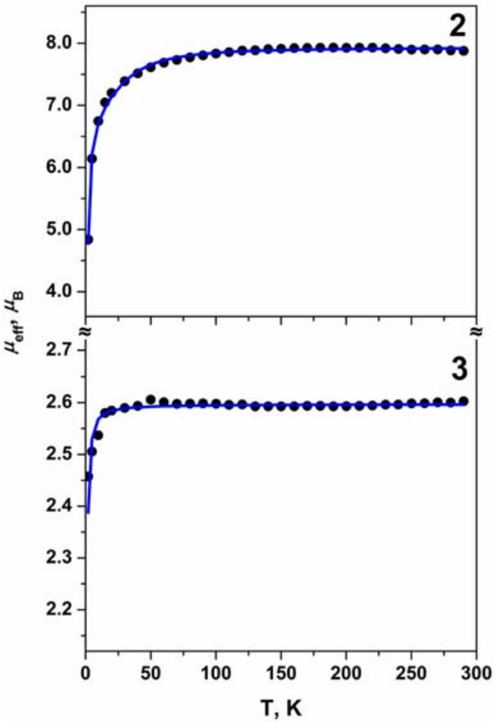

Figure 8. Temperature dependence of the magnetic moment μ_{eff}, μ_B, of powdered samples of **2** and **3**. Filled circles are experimental data; blue line represents the best fit. For **2**: $S_1 = S_2 = 2$, $g_1 = g_2$= 2.21, J = 0.043 cm^{-1}, |D_1| = |D_2| = 19.7 cm^{-1}, $E/D_1 = E/D_2$ = 0.26, TIP = 0.027 emu, including a 12% impurity with S = 2. For **3**: $S_1 = S_2 = 1/2$, g_1 = g_2= 2.12 (fixed), J = −0.241 cm^{-1}, TIP = 50 × 1e^{-6} emu.

transitions to resonant field positions beyond the available magnetic field (1.8 T).

The magnetic susceptibility data for **3** shows weak ferromagnetic coupling between the two Cu^{II} centers (Figure 8). The temperature-independent (20−290 K) effective magnetic moment of ~2.6 μ_B matches the expected value for two uncoupled Cu^{II} centers with the hallmark $g \approx 2.1$. Data were fit for g = 2.12 and J = −0.2 cm^{-1}. This very small exchange coupling precludes assignment of the total spin ground state in **3**, and therefore, J should be treated as an absolute value. The X-band EPR spectrum recorded in MeCN/CH$_2$Cl$_2$ displayed a signal consistent with the interpretation of the magnetic data, that is, two weakly coupled Cu^{II} (S = 1/2) ions (Figure 9). The spectral profile is dominated by a large g splitting synonymous with Cu^{II}; plus addition of the minuscule exchange coupling gives rise to a poorly resolved 7-line hyperfine pattern in the $g_{\parallel}$ region characteristic of coupled ^{63,65}Cu (I = 3/2, 100% abundant) nuclei. This pattern is more clearly displayed at K-band frequency (~24 GHz) where the enhanced Zeeman interaction separates the parallel component centered on $g_{\parallel}$ = 2.196 from the broad perpendicular feature at $g_{\perp} \approx 2.08$ that is devoid of hyperfine splitting (Figure S11, Supporting Information). The inset in Figure 9 shows a half-field feature arising from the forbidden "ΔM_S = 2" transition of the spin triplet (S = 1) formed by coupling of the two Cu^{II} ions. The 7-line pattern is poorly resolved as its intensity is proportional to the magnitude of D,[48,49] and therefore, substantially higher power (63 mW) was required to expose this feature.

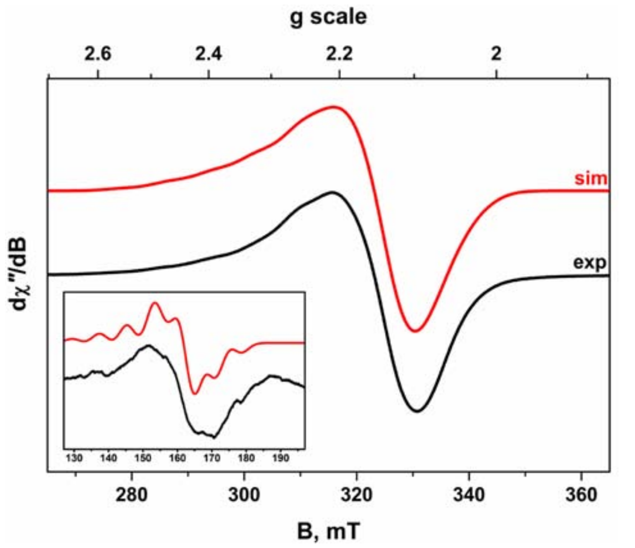

Figure 9. X-band EPR spectrum of **3** recorded in MeCN/CH$_2$Cl$_2$ at 10 K (experimental conditions: frequency, 9.4740 GHz; modulation, 0.2 mT; power, 0.2 mW). Experimental spectrum shown in black, and simulation depicted by the red trace: g = 2.081, 2.088, 2.196; A = 0, 40, 156 × 10^{-4} cm^{-1}; J = −0.2 cm^{-1} (fixed); $d_{Cu\cdots Cu}$ = 6.9 Å; χ = 34°; ρ = 7°. (Inset) Experimental and simulated EPR spectra in the half-field region (conditions: frequency, 9.4741 GHz; modulation, 1.0 mT; power, 63 mW).

Simulation of both the X- and the K-band spectrum was achieved with the same spin Hamiltonian parameters: g = (2.081, 2.088, 2.196) and A = (0, 40, 156) × 10^{-4} cm^{-1}. The spin−spin interaction was included in the simulation using a J interaction matrix, which incorporates both exchange and dipolar coupling elements. The best fit was achieved for J = −0.2 cm^{-1} (fixed from magnetic susceptibility) for an interspin distance (r) of 6.9 Å retrieved from the crystal structure and is consistent with very weakly coupled Cu^{II} ions. Inclusion of two Euler angles, χ = 34° and ρ = 7°, defined as the relative orientation of the local g axes which are mostly determined by the orientation of the magnetic orbital of the second Cu^{II} site with respect to the first and enabled the experimental hyperfine line shape to be successfully modeled. Simulation was less sensitive to the magnitude of ρ, and the χ angle is close to the crystallographically defined dihedral angle (∼40°) between the CuN_4 basal planes orthogonal to the Jahn−Teller axis. The zero-field splitting parameter, D, can be estimated from a two-point dipole model, $D = -(3/2)g^2\mu_B{}^2r^{-3} \approx -0.005$ cm^{-1}, a value consistent with the extremely weak half-field transition (Figure 9, inset).

Ferromagnetic interactions between the metal ions in **2** and **3** might be presupposed, based on previous studies with bimetallic phenylenediamine systems.[50,51] Ferromagnetic coupling is expected for systems containing an odd number of bridging atoms between two paramagnetic centers (i.e., with meta-substituted benzene linkers), while an even number of bridging atoms promotes antiferromagnetic interactions. Spectroscopic, magnetic, and DFT computational studies demonstrated that the coupling is orchestrated by spin polarization through the aromatic bridge. The magnitude of the exchange interactions in the Cu^{II} 1,3-[bis(2-pyridylmethyl)-amino]benzene complexes was further shown to be dependent on the orientation of the metal SOMOs with respect to the phenylenediamine unit.[50]

DFT calculations on **3**, likewise, illustrate spin polarization of the phenylenediamine system of **L**^{1}. The spin density map depicts an alternating pattern on the carbon atoms of the central aromatic ring, with delocalization of the metal spin toward the amino nitrogen of the bis(pyridylmethyl) group (Figure 10). The SOMOs of **3** (Figure 11) consist of the in-phase and out-of-phase σ^* orbitals, comprising ∼34% Cu d$_{x^2-y^2}$ character, directed toward the N$_{am}$ p orbital, with minor contributions from the π system of the benzene ring. However, due to the orientation of the α-iminopyridine ligands, the N$_{im}$ p orbitals lie orthogonal to the d$_{x^2-y^2}$-based σ^* orbitals, severing the conventional pathway for π-type exchange through the N$_{im}$−C−C−C−N$_{am}$ bridge. Efficient π-type overlap of the Cu SOMOs with *both* N p orbitals in the related 1,3-phenylenediamine bridged cupric metallocyclophane (Cu···Cu = 6.8 Å)[51] and 1,3-[bis(2-pyridylmethyl)amino]benzene complexes (Cu···Cu = 5.9 Å)[50] led to substantial coupling of the two metal centers, with measured exchange constants of 8.4 and 4.6 cm^{-1}, respectively, obtained from magnetic susceptibility measurements. Vanishing interactions between the metal ions in **3** can thus be attributed to the lack of a direct π-type pathway to connect the two Cu d$_{x^2-y^2}$ orbitals through one **L**^{1} molecule. Interactions between the stacked benzene rings of **L**^{1} might provide an alternate pathway for communication between the two copper centers.[52] Further inspection of the remaining metal-based MOs of **3** also reveals pervasive covalency, with contributions from the ligand π system and admixture of the copper d orbitals. Spin−orbit coupling contributions, therefore, might also account for the weak coupling in **3**.

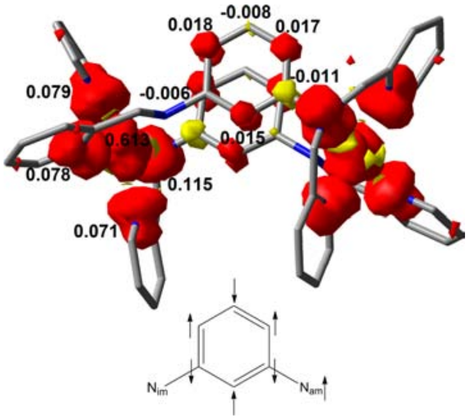

Figure 10. DFT-derived (B3LYP) spin density plot for **3** based on Löwdin population analysis.

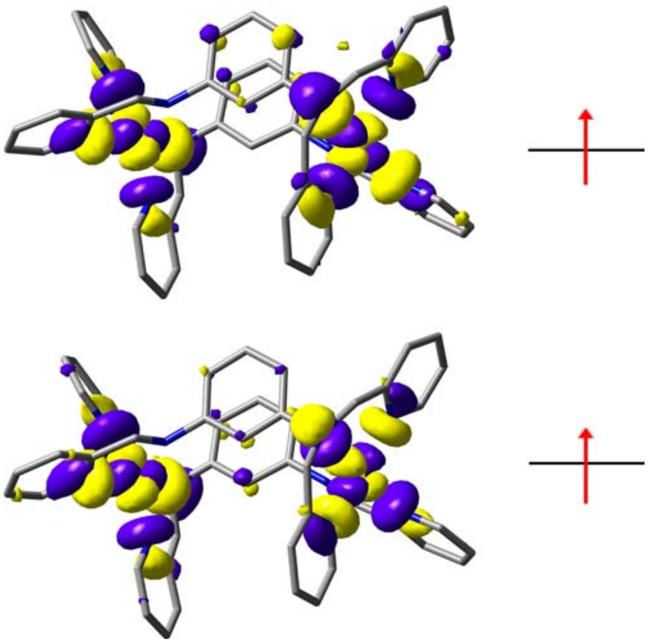

Figure 11. DFT-derived (B3LYP) SOMOs for **3**.

The iron centers in **2** are essentially uncoupled. Several factors impede strong communication between the iron sites, as illustrated by both the molecular structure and the DFT calculations.[53] The metal separation (7.5−7.7 Å) is substantially greater than that in **3**. The α-iminopyridine is canted at 24° (**2′**) or 52° (**2**) with respect to the plane of the benzene bridge, which results in poor overlap with the aromatic π system. The DFT-derived spin density map for **2** (Figure 12) depicts negligible spin density on the phenylenediamine unit, and in contrast to **3**, all SOMOs are strongly metal based. Overlap between the Fe d$_{z^2}$ orbitals and the extended N$_{im}$−C−C−C−N$_{am}$ π system (Figure 13) provides a possible exchange pathway between the iron centers. However, the benzene π system contributes minimally to these d$_{z^2}$-based SOMOs.

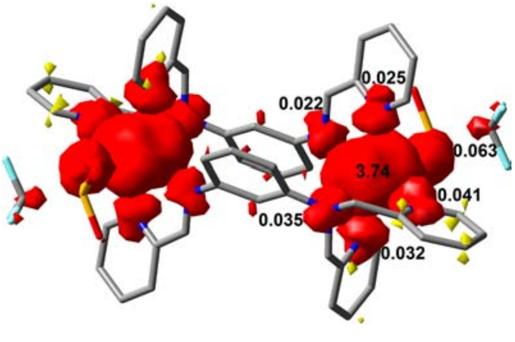

Figure 12. DFT-derived (B3LYP) spin density plot for **2** based on Löwdin population analysis.

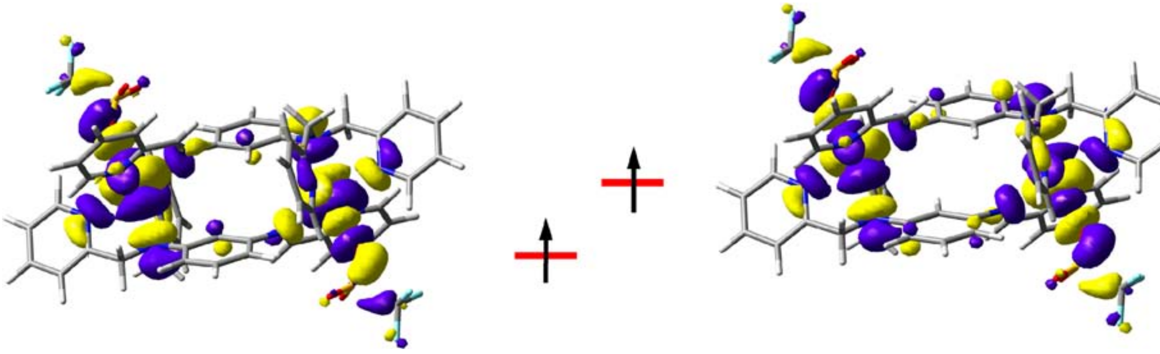

Figure 13. DFT-derived (B3LYP) Fe d_{z^2}-based SOMOs for **2**.

CONCLUSIONS

The new ligand, **L**^{1}, provides a platform for bimetallic complexes, with multiple redox sites furnished by the terminal α-iminopyridine moiety. The high flexibility of the ligand accommodates the coordination geometry preferences of various metal ions and formation of both symmetric and asymmetric binuclear complexes. Electrochemical studies confirm the redox activity of **L**^{1} and provide an indication of the nature of the reductive processes available to the bimetallic compounds. The redox behavior of **1**−**3** appears to follow the anticipated trend for the series of metals examined in this study. One-electron reduction of the ligand is observed for **1**, in which **L**^{1} is coordinated to redox-inert Zn^{II}, whereas reduction of the dimeric copper complex, **3**, likely involves the Cu$^{II/I}$ couple. A second reduction event only is observed in the CV of **2**, which is the most intriguing of the three metal compounds that we isolated. Compound **2** offers the option of both metal- and ligand-centered redox processes; the ensuing spin coupling can lead to varied electronic structures.

Both **2** and **3** are paramagnetic. The coordination of the triflate ions in **2** supports a high-spin configuration at each Fe^{II} center. While studies have shown that 1,3-phenylenediamine bridges in related binuclear compounds can provide an efficient route for exchange interactions between two metal centers, the metal ions in both **2** and **3** are virtually uncoupled. Inspection of the molecular structures and calculated data reveals that the communication pathway between the metal sites is dismantled by the orientation of the phenylenediamine groups and the coordination geometry adopted by the metal. As a result, **L**^{1} may provide a means to localize charge upon reduction of the compounds. Efforts are currently underway to isolate and characterize the reduced forms of the **L**^{1}−metal complexes.

ASSOCIATED CONTENT

Supporting Information

Crystallographic data files (CIF format), additional electrochemical, spectroscopic, and computational data, and NMR spectra of new compounds. This material is available free of charge via the Internet at http://pubs.acs.org.

AUTHOR INFORMATION

Corresponding Author

*E-mail: c.r.hess@durham.ac.uk.

Notes

The authors declare no competing financial interest.

ACKNOWLEDGMENTS

We thank the EPSRC, the University of Durham, and the Durham Energy Institute for financial support. We are grateful to Mr. Bernd Mienert (MPI) for technical assistance with Mössbauer and SQUID measurements. We thank Dr. Alan Kenwright for helpful discussions concerning NMR experiments and Prof. Andy Beeby for the use of his instrument for diffuse reflectance spectra.

REFERENCES

(1) Chirik, P. J. *Inorg. Chem.* **2011**, *50*, 9737.

(2) Sproules, S.; Wieghardt, K. *Coord. Chem. Rev.* **2011**, *255*, 837.

(3) Kaim, W. *Eur. J. Inorg. Chem.* **2012**, 343.

(4) Hindson, K.; de Bruin, B. *Eur. J. Inorg. Chem.* **2012**, 340.

(5) Haneline, M.; Heyduk, A. F. *J. Am. Chem. Soc.* **2006**, *128*, 8410.

(6) Sylvester, K. T.; Chirik, P. J. *J. Am. Chem. Soc.* **2009**, *131*, 8772.

(7) Tondreau, A. M.; Milsmann, C.; Patrick, A. D.; Hoyt, H. M.; Lobkovsky, E.; Wieghardt, K.; Chirik, P. J. *J. Am. Chem. Soc.* **2010**, *132*, 15046.

(8) Kraft, S. J.; Williams, U. J.; Daly, S. R.; Schelter, E. J.; Kozimor, S. A.; Boland, K. S.; Kikkawa, J. M.; Forrest, W. P.; Christensen, C. N.; Schwarz, D. E.; Fanwick, P. E.; Clark, D. L.; Conradson, S. D.; Bart, S. C. *Inorg. Chem.* **2011**, *50*, 9838.

(9) Ouch, K.; Mashuta, M. S.; Grapperhaus, C. A. *Inorg. Chem.* **2011**, *50*, 9904.

(10) Nguyen, A. I.; Zarkesh, R. A.; Lacy, D. C.; Thorson, M. K.; Heyduk, A. F. *Chem. Sci.* **2011**, *2*, 166.

(11) Kaim, W. *Inorg. Chem.* **2011**, *50*, 9752.

(12) Nawn, G.; Waldie, K. M.; Oakley, S. R.; Peters, B. D.; Mandel, D.; Patrick, B. O.; McDonald, R.; Hicks, R. G. *Inorg. Chem.* **2011**, *50*, 9826.

(13) Arumugam, K.; Shaw, M. C.; Chandrasekaran, P.; Villagran, D.; Gray, T. G.; Mague, J. T.; Donahue, J. P. *Inorg. Chem.* **2009**, *48*, 10591.

(14) Hess, C. R.; Weyhermüller, T.; Bill, E.; Wieghardt, T. *Angew. Chem., Int. Ed.* **2009**, *48*, 3703.

(15) Szigethy, G.; Heyduk, A. F. *Inorg. Chem.* **2011**, *50*, 125.

(16) Zarkesh, R. A.; Ziller, J. W.; Heyduk, A. F. *Angew. Chem., Int. Ed.* **2008**, *47*, 4715.

(17) Lu, C. C.; Bill, E.; Weyhermüller, T.; Bothe, E.; Wieghardt, K. *J. Am. Chem. Soc.* **2008**, *130*, 3181.

(18) Parkin, G. *J. Chem. Educ.* **2006**, *83*, 791.

(19) Hah, J.-M.; Martásek, P.; Roman, L. J.; Silverman, R. B. *J. Med. Chem.* **2003**, *46*, 1661.

(20) Hanson, G. R.; Gates, K. E.; Noble, C. J.; Griffin, M.; Mitchell, A.; Benson, S. *J. Inorg. Biochem.* **2004**, *98*, 903.

(21) Cosier, J.; Glazer, A. M. *J. Appl. Crystallogr.* **1986**, *19*, 105.

(22) *APEX2, X-ray software suite*, version 2012.4-3; Bruker Analytical X-ray Instruments Inc.: Madison, WI, 2012.

(23) *SAINT, Data Reduction Software*, version 8.18c; Bruker Analytical X-ray Instruments Inc., Madison, WI, 2012.

(24) Dolomonov, O.; Bourhis, L. J.; Gildea, R. J.; Howard, J. A. K.; Puschmann, H. *J. Appl. Crystallogr.* **2009**, *42*, 339.

(25) Sheldrick, G. M. *J. Acta Crystallogr., Sect A: Found. Crystallogr.* **2008**, *64*, 112.

(26) Neese, F. *An Ab initio, DFT and Semiempirical SCF-MO Package*, Version 2.9; Max Planck Institute for Bioinorganic Chemistry, Mülheim an der Ruhr, Germany, Jan 2012.

(27) Becke, A. D. *J. Chem. Phys.* **1986**, *84*, 4524.

(28) Becke, A. D. *J. Chem. Phys.* **1993**, *98*, 5648.

(29) Lee, C. T.; Yang, W. T.; Parr, R. G. *Phys. Rev. B* **1988**, *37*, 785.

(30) Schäfer, A.; Horn, H.; Ahlrichs, R. *J. Chem. Phys.* **1992**, *97*, 2571.

(31) Schäfer, A.; Huber, C.; Ahlrichs, R. *J. Chem. Phys.* **1994**, *100*, 5829.

(32) Eichkorn, K.; Treutler, O.; Ohm, H.; Häser, M.; Ahlrichs, R. *Chem. Phys. Lett.* **1995**, *240*, 283.

(33) Eichkorn, K.; Treutler, O.; Öhm, H.; Häser, M.; Ahlrichs, R. *Chem. Phys. Lett.* **1995**, *242*, 652.

(34) *GaussView 4.1.2*; Gaussian, Inc.: Wallington, CT, 2006.

(35) Hess, C. R.; Weyhermüller, T.; Bill, E.; Wieghardt, T. *Inorg. Chem.* **2010**, *49*, 5686.

(36) Ray, K.; Petrenko, T.; Wieghardt, K.; Neese, F. *Dalton Trans.* **2007**, 1552.

(37) Ward, A. L.; Elbaz, L.; Kerr, J. B.; Arnold, J. *Inorg. Chem.* **2012**, *51*, 4694.

(38) England, J.; Gondhia, R.; Bigorra-Lopez, L.; Peterson, A. R.; White, A. J. P.; Britovsek, G. J. P. *Dalton Trans.* **2009**, 5319.

(39) Börzel, H.; Comba, P.; Hagen, K. S.; Lampeka, Y. D.; Lienke, A.; Linti, G.; Merz, M.; Pritkow, H.; Tsymbal, L. V. *Inorg. Chim. Acta* **2002**, *337*, 407.

(40) Schindler, S.; Szalda, D. J.; Creutz, C. *Inorg. Chem.* **1992**, *31*, 2255.

(41) Murthy, N. N.; Mahroof-Tahir, M.; Karlin, K. D. *Inorg. Chem.* **2001**, *40*, 628.

(42) Compton, R. G.; Banks, C. E. *Understanding Voltammetry*; 2nd ed.; Imperial College Press: London, 2011.

(43) Muresan, N.; Lu, C. C.; Ghosh, M.; Peters, J. P.; Abe, M.; Henling, L. M.; Weyhermüller, T.; Bill, E.; Wieghardt, K. *Inorg. Chem.* **2008**, *47*, 4579.

(44) Foxon, S.; Xu, J.-Y.; Turba, S.; Leibold, M.; Hampel, F.; Heinemann, F. W.; Walter, O.; Würtele, C.; Holthausen, M.; Schindler, S. *Eur. J. Inorg. Chem.* **2007**, 429.

(45) $\tau = 0$ represents a perfect square pyramid, $\tau = 1$ corresponds to perfectly trigonal bipyramidal geometry. See: Addison, A. W.; Rao, T. N.; Reedijk, J.; van Rijn, J.; Verschoor, G. C. *J. Chem. Soc., Dalton Trans.* **1984**, 1349.

(46) Greenwood, N. N.; Gibb, T. C. *Mössbauer Spectroscopy*; Chapman and Hall Ltd.: London, 1971.

(47) A reasonable fit of the data could only be obtained by including a TIP value of 0.027 emu, which is unlikely to correspond to temperature-independent paramagnetism of the diiron complex. The Mössbauer spectrum of the bulk solid (Figure S10, Supporting Information) shows the presence of a second iron-containing species in the powder samples. The presence of the secondary component has been taken into account in the fit of the magnetic data (12%, $S = 2$) but does not account for the large TIP values. Although we do not know the origin, the TIP-like background magnetism suggests the presence of magnetic nanoparticles that constitute a minor component of bulk solid samples of **2**.

(48) Eaton, S. S.; More, K. M.; Sawant, B. M.; Eaton, G. R. *J. Am. Chem. Soc.* **1983**, *105*, 6560.

(49) Eaton, S. S.; Eaton, G. R. *Coord. Chem. Rev.* **1988**, *83*, 29.

(50) Foxon, S. P.; Torres, G. R.; Walter, O.; Pederson, J. Z.; Toftlund, H.; Hüber, M.; Falk, K.; Haase, W.; Cano, J.; Lloret, F.; Julve, M.; Schindler, S. *Eur. J. Inorg. Chem.* **2004**, 335.

(51) Fernández, I.; Ruiz, R.; Faus, J.; Julve, M.; Lloret, F.; Cano, J.; Ottenwaelder, X.; Journaux, Y.; Muñoz, M. C. *Angew. Chem., Int. Ed.* **2001**, *40*, 3039.

(52) Martín, S.; Grace, I.; Bryce, M. R.; Wang, C.; Jitchati, R.; Batsanov, A. S.; Higgins, S. J.; Lambert, C. J.; Nichols, R. J. *J. Am. Chem. Soc.* **2010**, *132*, 9157.

(53) DFT calculations were carried out on both solvatomorphs of **2** and yielded identical results (see Supporting Information).